Stress–strain behavior of ferrite and bainite with nano-precipitation in low carbon steels

Naoya Kamikawa,[a,*] Kensuke Sato,[b] Goro Miyamoto,[a] Mitsuhiro Murayama,[c] Nobuaki Sekido,[d] Kaneaki Tsuzaki[e] and Tadashi Furuhara[a]

[a]*Institute for Materials Research, Tohoku University, 2-1-1 Katahira, Aoba-ku, Sendai 980-8577, Japan*
[b]*Graduate Student, Tohoku University, 2-1-1 Katahira, Aoba-ku, Sendai 980-8577, Japan*
[c]*Department of Materials Science and Engineering, Virginia Tech, Blacksburg, VA 24061, USA*
[d]*National Institute for Materials Science, 1-2-1 Sengen, Tsukuba, Ibaraki 305-0047, Japan*
[e]*Department of Mechanical Engineering Science, Kyushu University, 744 Motooka, Nishi-ku, Fukuoka 819-0395, Japan*

Abstract—We systematically investigate stress–strain behavior of ferrite and bainite with nano-sized vanadium carbides in low carbon steels; the ferrite samples were obtained through austenite/ferrite transformation accompanied with interphase precipitation and the bainite samples were via austenite/bainite transformation with subsequent aging. The stress–strain curves of both samples share several common features, i.e. high yield stress, relatively low work hardening and sufficient tensile elongation. Strengthening contributions from solute atoms, grain boundaries, dislocations and precipitates are calculated based on the structural parameters, and the calculation result is compared with the experimentally-obtained yield stress. The contributions from solute atoms and grain boundaries are simply additive, whereas those from dislocations and precipitates should be treated by taking the square root of the sum of the squares of two values. Nano-sized carbides may act as sites for dislocation multiplication in the early stage of deformation, while they may enhance dislocation annihilation in the later stage of deformation. Such enhanced dynamic recovery might be the reason for a relatively large elongation in both ferrite and bainite samples.
© 2014 Acta Materialia Inc. Published by Elsevier Ltd. All rights reserved.

1. Introduction

Strength and other mechanical properties of metals and alloys are designed by controlling lattice defects in crystals. Crystal defects that affect the mechanical properties of materials are mainly dislocations, solute atoms, precipitates and grain boundaries, all of which generally act as obstacles for dislocation movement during deformation at relatively low temperature, leading to an increase in strength of materials. Strengthening by dislocations, solute atoms, precipitates and grain boundaries are termed dislocation strengthening, solid solution strengthening, precipitation strengthening and grain boundary strengthening, respectively. Among these strengthening mechanisms, much attention has recently been paid to precipitation strengthening in steel production.

It is well known that precipitation strengthening by undeformable hard particles increases inversely proportional to the average inter-particle spacing, according to the Orowan mechanism [1]:

$$\tau_{ppt} \propto \frac{Gb}{L} \ (\text{MPa}) \tag{1}$$

where τ_{ppt} is the contribution from precipitation strengthening in shear stress, G is the shear modulus, b is the Burgers vector and L is the inter-particle spacing. Note that the inter-particle spacing L is an increasing function against the average radius of particles or a decreasing function against the volume fraction of particles [2] (see also Eq. (15) in this paper). In other words, a decrease in average size or an increase in volume fraction of particles leads to an increase in precipitation strengthening in the Orowan-type precipitation strengthening. However, too much addition of expensive alloying elements to obtain high volume fraction of particles unwantedly results in a significant increase in the production cost. Therefore, dispersion of nano-sized precipitates, or nano-precipitation (see e.g. Refs. [3,4]), is a promising strategy to maximize precipitation strengthening with minimizing the addition of alloying elements. This is one of the main reasons why nano-precipitation has

* Corresponding author. Tel.: +81 22 215 2048; fax: +81 22 215 2046; e-mail: kamikawa@imr.tohoku.ac.jp

recently received much attention in the production of high-strength steels.

In carbon steels containing strong carbide-forming elements, such as niobium, titanium and vanadium, nano-sized alloy carbides can be formed and dispersed into the matrix during heat treatments, either by interphase precipitation or by tempering of martensite and bainite. In interphase precipitation [5–9], nano-sized alloy carbides are nucleated on austenite/ferrite interfaces during ferrite transformation from austenite, typically leaving a periodic array of alloy carbides in the ferrite. One of the advantages of interphase precipitation is that high-strength ferrite steels can be produced directly during cooling from austenite at high temperature, so that subsequent heat treatment is not necessary, i.e. heat treatment cost can be reduced, unlike quenched martensite steels that require tempering. Low and medium carbon steels with interphase precipitated carbides are known to show high strength and good formability, so that such steels have been in practical use, mainly as automobile body parts [10–13]. On the other hand, high-temperature tempering of martensite or bainite in alloy steels can also produce precipitation of nano-sized alloy carbides, leading to an increase in strength during tempering, which is called secondary hardening [14–19]. Secondary hardened martensite or bainite steels have also been used widely in industrial applications, such as tool and die steels or automobile products, because of its ultrahigh strength and sufficient toughness.

Although steels containing nano-sized alloy carbides have widely been used in commercial applications, the effect of nano-sized alloy carbides on mechanical properties is still unclear. This study will focus on the effect of nano-sized carbides on strength and ductility in different ferrite matrices. Fig. 1 schematically shows microstructures obtained by interphase precipitation (a), and by aging of martensite or bainite (b), both containing nano-sized alloy carbides. In interphase precipitation (Fig. 1a), nano-sized carbides are precipitated in the matrix of polygonal ferrites with a low density of dislocations. On the other hand, in aging of martensite or bainite (Fig. 1b), nano-sized carbides

are dispersed in elongated martensite lathes or bainitic ferrites with high density of dislocations. The effect of nano-sized alloy carbides on the mechanical properties of materials could be different between these two cases, but details are not yet understood very well.

In the present study, therefore, ferrite and bainite structures with nano-sized carbides are prepared using a low carbon steel containing a small amount of vanadium. Uniaxial tensile tests are systematically carried out at room temperature, and the effect of nano-precipitates on yield stress, work hardening and ductility is discussed in detail.

2. Experimental

A low carbon steel with a chemical composition of Fe–0.10C–0.22Si–0.83Mn–0.014P–0.014S –0.003 N–0.001Ti–0.288V (in mass%) was used in the present study. From thermodynamic calculation by Thermo-Calc software, the following temperatures were obtained: vanadium carbide (VC) solution temperature of 1077 °C, Ae_3 temperature of 852 °C and Ae_1 temperature of 713 °C in para-equilibrium. A cast ingot of the steel prepared by vacuum melting was hot-rolled at the finish rolling temperature of ∼940 °C. Hot-rolled samples were homogenized in Ar atmosphere at 1180 °C for 24 h, and were used as starting materials. The starting materials were heat-treated in a vacuum furnace at 1200 °C for 600 s for austenitization and solution treatment, and immediately isothermally transformed at 690 °C or 600 °C in a salt bath for different holding periods in the range from 20 s to 172.8 ks (48 h), followed by water quenching. The isothermal treatment temperature of 690 °C was chosen to obtain ferrite structure with interphase precipitation of nano-sized VC particles, while the temperature of 600 °C was chosen to obtain bainite structure with precipitation of VC particles by aging.

Microstructures of the obtained samples were characterized by optical microscopy, electron backscatter diffraction (EBSD) in a scanning electron microscope (SEM) and transmission electron microscopy (TEM). Longitudinal sections perpendicular to transverse direction (TD) (TD planes), including rolling direction (RD) and normal direction (ND), of the hot-rolled sheets were prepared for the observations. For optical microscopy and EBSD measurements, TD planes were mechanically polished by SiC emery papers, diamond paste and then colloidal silica to obtain mirror surfaces, followed by etching in a solution of 3 vol.% HNO_3 (nitric acid) + 97 vol.% C_2H_5OH (ethanol). EBSD measurements were carried out in an FEI Quanta 3D SEM using a program TSL OIM Dara Correction. The obtained data were analyzed using a program TSL OIM Analysis. For TEM observations, thin foils parallel to TD planes were mechanically polished by SiC emery papers and then electro-polished in a solution of 10 vol.% $HClO_4$ (perchloric acid) + 90 vol.% C_2H_5OH (ethanol) at −15 °C at a voltage of 40 V. Conventional bright field (BF) and dark field (DF) images were taken by an FEI CM300 TEM operating at 300 kV. Dislocation density in the samples was determined from TEM images taken under multi-beam diffraction conditions to reveal all dislocations, where the thickness of the TEM foils was measured by the convergent beam electron diffraction technique. High resolution TEM observation was also carried out in an FEI Titan 300 operating at 300 kV, to observe atomic structures of ferrite matrix and precipitates.
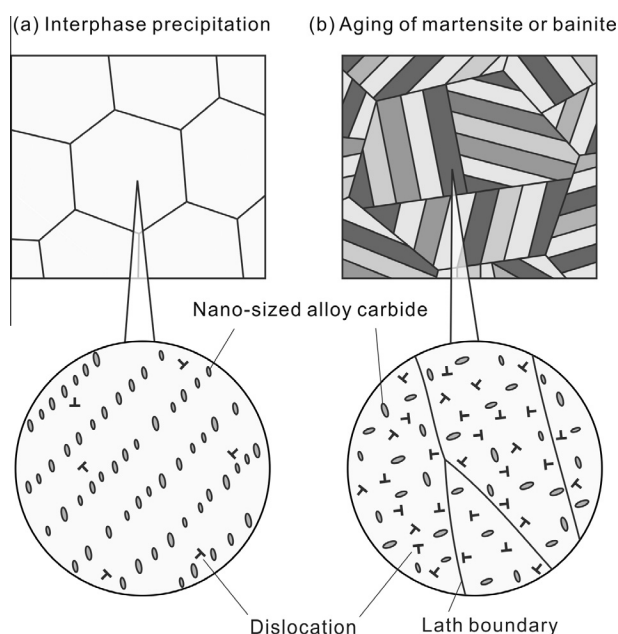

Fig. 1. Schematic illustration of microstructures obtained by interphase precipitation (a) or by aging of martensite or bainite (b).

To quantify the VC particle size, dark field TEM observation was applied for VC particles. It is well known that VC particles with the sodium chloride (NaCl) type (or B1-type) structure generally precipitate in the body centered cubic (bcc) ferrite (α) matrix with the Baker–Nutting relationship [20] described as

$$(100)_{VC}//(100)_\alpha$$
$$[010]_{VC}//[011]_\alpha \qquad (2)$$

In the Baker–Nutting orientation relationship, there are three possible variants to be precipitated. In precipitation by aging, all of three variants would be possible, while in interphase precipitation only one variant of alloy carbide, whose $\{100\}_{VC}$ habit plane is nearly parallel to the austenite/ferrite interface, preferentially forms [5]. To highlight the VC particles in the DF imaging mode, the incident beam direction was set almost parallel to $[001]$ of ferrite matrix, and dark field images were taken under a diffraction condition of $g^* = 200_{VC}$. From the obtained dark field images, the average diameter of VC particles was measured. Assuming that VC particles have a morphology of oblate spheroid with the habit plane parallel to the $[100]$ plane of ferrite, the volume of oblate spheroid was calculated. The diameter of the VC particle was defined as a diameter of sphere that has the same volume as the oblate spheroid. The experimental details of TEM observation and particle size determination are described elsewhere [21,22].

The serial sectioning method using a field-emission (FE) SEM equipped with a focused ion beam (FIB) system was applied to reconstruct three-dimensional (3-D) images of interphase precipitation of VC particles. A characteristic feature of the FIB/FE-SEM dual-beam microscope used in this study is an orthogonal arrangement of FIB and FE-SEM optics, by which high-resolution SEM images with uniform background intensity can be obtained [23]. The slice step of FIB sectioning was 5 nm, and SEM images were taken at an acceleration voltage of 1 kV with an in-lens detector. The SEM images obtained by serial sectioning were three-dimensionally reconstructed by a commercial software package Avizo.

Mechanical properties of the samples were evaluated by the Vickers hardness test and tensile test at room temperature. Hardness tests were carried out using a Matsuzawa MHT-1 hardness tester at a load of 1 kgf for a holding period of 15 s. At least 10 hardness values were obtained and averaged. To obtain stress–strain curves, tensile tests were carried out at room temperature. Tensile specimens with a gauge length of 10 mm, a gauge width of 5 mm and a thickness of 1 mm were prepared with the tensile axis parallel to thte RD of the hot-rolled sheets. Tensile tests were carried out using Shimadzu AG-5000B at a constant crosshead speed of 0.5 mm min^{-1}, corresponding to an initial strain rate of 8.3×10^{-4} s^{-1}. Tensile elongations were determined by a clip-on extensometer.

3. Results

3.1. Microstructural characterization

In this work, two different series of heat treatments were carried out after austenitization at 1200 °C: (i) isothermal transformation treatment at 690 °C to obtain ferrite structures and (ii) isothermal transformation treatment at 600 °C to obtain bainite structures. For each condition, microstructures were characterized by optical microscopy, EBSD and TEM.

3.1.1. Ferrite transformation with interphase precipitation
3.1.1.1. Optical microstructures. Fig. 2 shows the optical microstructures of the samples transformed at 690 °C. By holding for 20 s (Fig. 2a), polygonal or allotriomorphic ferrites are nucleated mainly at austenite grain boundaries. The volume fraction of ferrite increases with increasing the holding period, and the ferrite transformation is almost completed after the holding for 300 s (Fig. 2c). Note that pearlite structure can be seen in this 300 s holding sample, and cementites in the pearlite are spheroidized for longer-time holding above 10 h. However, the volume fraction of the cementite structure is determined
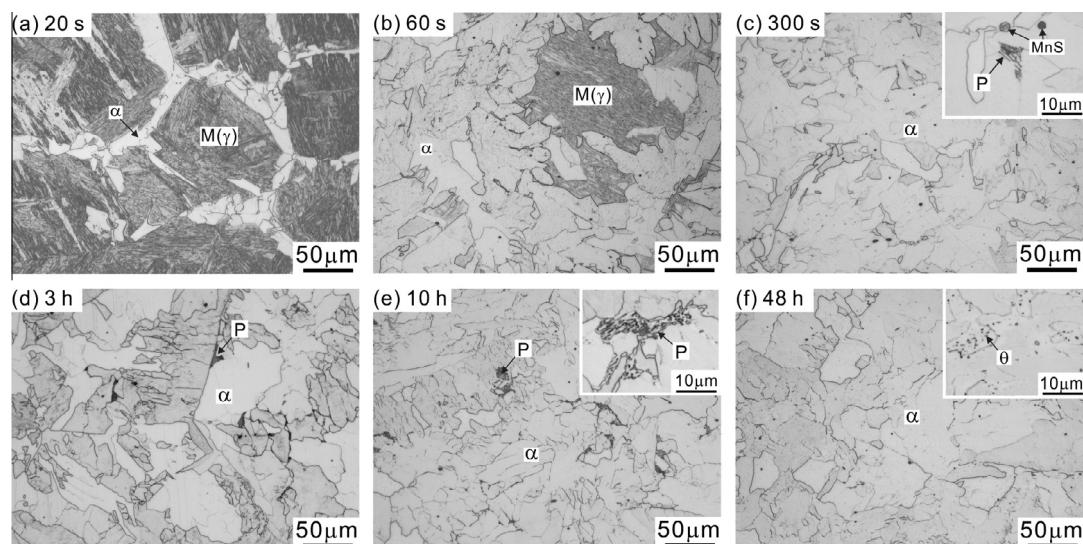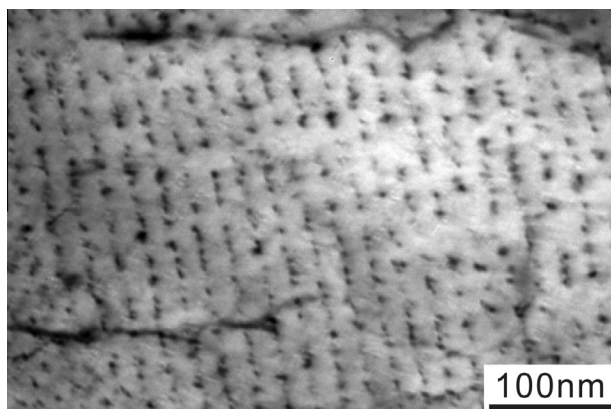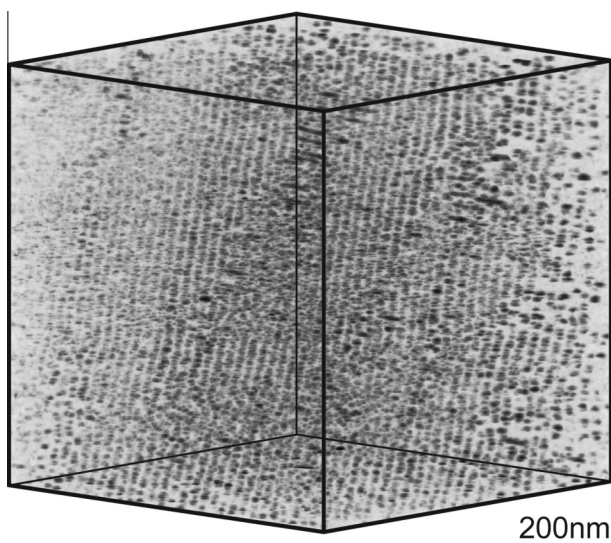

Fig. 2. Optical microstructures of the samples isothermally transformed at 690 °C for different holding periods: (a) 20 s, (b) 60 s, (c) 300 s, (d) 3 h, (e) 10 h and (f) 48 h.

Fig. 3. Bright field TEM image of the sample isothermally transformed at 690 °C for 300 s, showing periodic sheets on which vanadium carbides are dispersed.

Fig. 4. 3-D view of the microstructure of the sample isothermally transformed at 690 °C for 300 s. A series of the SEM images has been taken by the serial sectioning method, and a 3-D image with a volume of 1 μm × 1 μm × 1 μm has been constructed. In the image, the VC particles are denoted by dark contrast while the ferrite matrix is transparent.

to be as small as ~1%, and therefore it can be assumed that the effect of such pearlite formation on the mechanical properties is negligible. EBSD measurements were carried out for the samples transformed by 300 s and 48 h holding, and the average ferrite grain size was determined to be ~29 μm for both cases, where boundaries with misorientation angles above 2° were taken into account for the grain size determination. This indicates that there was no significant grain growth of ferrite during long-time holding until 48 h.

3.1.1.2. TEM structures. Precipitation structures of the sample transformed by 300 s holding were observed by TEM, in which the ferrite transformation has almost completed. Fig. 3 is a bright field image of the sample, showing a periodic array of fine VC particles, which is typical of interphase precipitation alloy carbides. The average sheet
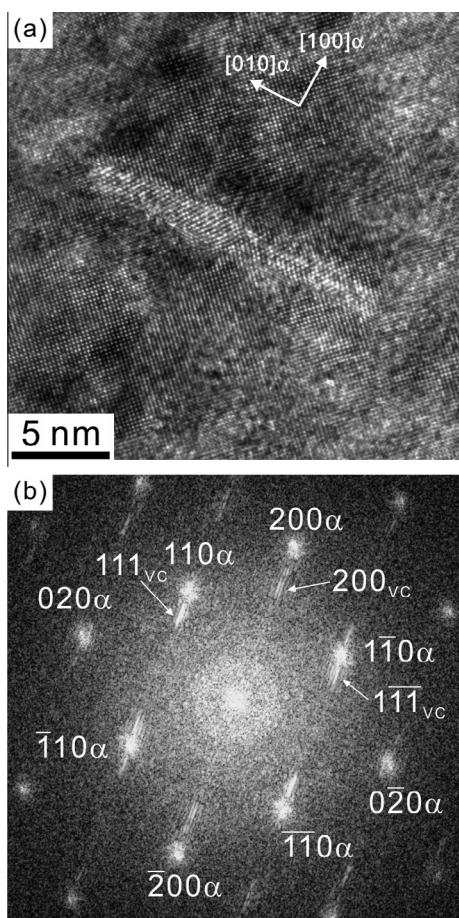
spacing of VC interphase precipitation was measured to be ~20–30 nm in this sample. A 3-D image reconstruction method using the FIB/FE-SEM technique has also confirmed that VC particles are distributed on sheets in the three dimensions. Fig. 4 demonstrates one example of the reconstructed image, which is an edge-on view of interphase precipitation sheets, i.e. the sheet plane is almost parallel to the observation direction. The periodic sheets of VC particles can be observed indeed, although the precipitation sheets are not completely flat but slightly curved. Note that such characteristic sheet-like morphology is not always formed in interphase precipitation, but in many cases nano-precipitates are distributed randomly. This tendency has been verified by 3-D atom probe tomography [24], where both sheet-like and random distribution of alloy carbides have been observed in the interphase precipitation of VC in a low carbon steel, suggesting that whether precipitation morphology becomes sheet-like or random strongly depends on the crystallographic characteristics of interfaces between parent austenite and transformed ferrite. Anyway, the above observation clearly proves that ferrite transformation accompanied with interphase precipitation of VC particles occurred in the isothermal holding at 690 °C, leading to a ferrite single phase structure with nano-sized VC particles.

High resolution TEM observation has also been carried out for this sample to reveal the crystal structures of ferrite matrix and VC particles. Fig. 5a shows a representative high resolution TEM image of a VC particle precipitated in the ferrite matrix. This image was taken under the condition where the incident beam was aligned to $[001]$ of ferrite matrix. The indexing of the diffractogram obtained by fast Fourier transformation (FFT) of the image (Fig. 5b) confirms that $[200]_\alpha$ is parallel to $[200]_{VC}$ and $[020]_\alpha$ is parallel to $[022]_{VC}$, i.e. the Baker–Nutting orientation relationship has been established. Since the habit plane of VC is $(100)_{VC}$, 3-D morphology of VC is disk-shaped, and Fig. 5a corresponds to an edge-on view of a disk-shaped particle.

To quantify the diameter of VC particles, dark field images were taken by conventional TEM for samples transformed at 690 °C, under a diffraction condition of $g^* = 200_{VC}$ in Fig. 6. Nano-sized VC particles are observed in the holding time of 300 s (Fig. 6a). The average diameter of the VC particles is determined to be 4.5 nm for this condition. The carbide size increases with increasing the holding period at 690 °C, and the average diameter becomes as large as 13 nm after 48 h holding (Fig. 6b and c). Variant analysis has been carried out for these samples by using the method described in Refs. [21,22], and it has been confirmed that one variant among three possible variants of VC is dominant in all cases, corresponding well with the previous reports [5,22].

3.2.1. Bainite transformation and subsequent aging
3.2.1.1. Optical microstructures. Optical observation was also carried out for samples transformed at 600 °C after different holding periods (Fig. 7). In the 20 s holding sample (Fig. 7a), although some equiaxed ferrite grains can be observed at austenite grain boundaries, lath-shaped bainitic ferrites are formed in the majority of the sample. The fraction of bainitic ferrites increases with increasing the holding period (Fig. 7b and c), and the holding for 3 h almost completes the transformation. As for the 690 °C holding, a small amount of pearlite structure can

Fig. 5. High resolution TEM image (a) and corresponding diffractogram obtained by FFT (b) of the sample isothermally transformed at 690 °C for 300 s. The image was taken under a beam condition parallel to [001] of ferrite matrix.
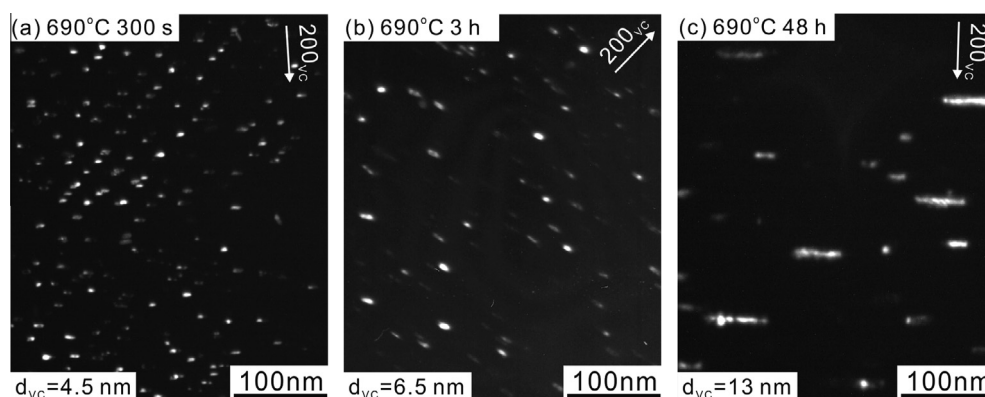
clearly showing a mixture of bainite structure (white contrast) and martensite structure (black contrast). Fig. 8b is a higher-magnification image of bainite structure region, which is characterized by lath-shaped bainitic ferrites with a high density of dislocations. These TEM images together with the optical microscopy images in Fig. 7 clearly confirm that the transformation at 600 °C led to bainitic transformation in this sample. Similar microstructural characteristics were observed in the bainitic ferrite regions of the samples transformed for a longer period until 48 h. The average width of bainitic lathes was measured to be ~1 μm, and the dislocation density inside the bainitic ferrites was measured to be 1.2–1.6×10^{14} m^{-2} in all cases.

Precipitation structures within bainitic ferrites were observed by the dark field imaging method. Dark field TEM images in Fig. 9 were taken under a diffraction condition of $g^* = 200_{VC}$ (//$200_{\alpha\text{-Fe}}$). There is no precipitate observed after 300 s holding (Fig. 9a). An additional observation was carried out under the diffraction condition of $g^* = 200_{VC}$ (//$020_{\alpha-Fe}$), but no precipitate was observed in this condition. Therefore, it seems that carbon and vanadium atoms are still supersaturated in the bainitic ferrite matrix after the 300 s holding. However, a prolonged holding for 3 h or a longer period leads to a precipitation of nano-sized VC particles, as shown in Fig. 9b and c. It has been confirmed that the observation under a diffraction condition of $g^* = 200_{VC}$ (//$020_{\alpha-Fe}$) also reveals nano-sized precipitates in these samples. These results indicate that such nano-sized alloy carbides were precipitated by aging during long-time holding after bainite transformation. Careful observations in TEM have found that many of VC particles are precipitated on dislocations or lath boundaries that act as preferential nucleation sites in the bainitic ferrite structure, but VC particles precipitated within bainitic ferrite matrix are also observed quite often. The average diameter of VC particles was determined to be 3.2 nm in the 3 h holding, and was slightly coarsened to 5.0 nm by the 48 h holding.

3.3. Mechanical properties

3.3.1. Vickers hardness

To understand the relationship between precipitation behavior observed above and the strength of the samples, macroscopic hardness was measured by a Vickers hardness tester for the samples transformed at 690 °C and 600 °C. The hardness is plotted as a function of holding period in

be observed after 3 h holding (Fig. 7d), but the volume fraction is negligibly small. Further holding leads to the spheroidization of pearlites (Fig. 7e and f).

3.2.1.2. TEM microstructures. Fig. 8 shows a microstructure of the sample transformed after 300 s, which is a mixture of bainite structure and a small amount of martensite that had been untransformed austenite before quenching (see Fig. 7c). Fig. 8a is a relatively low-magnification image,
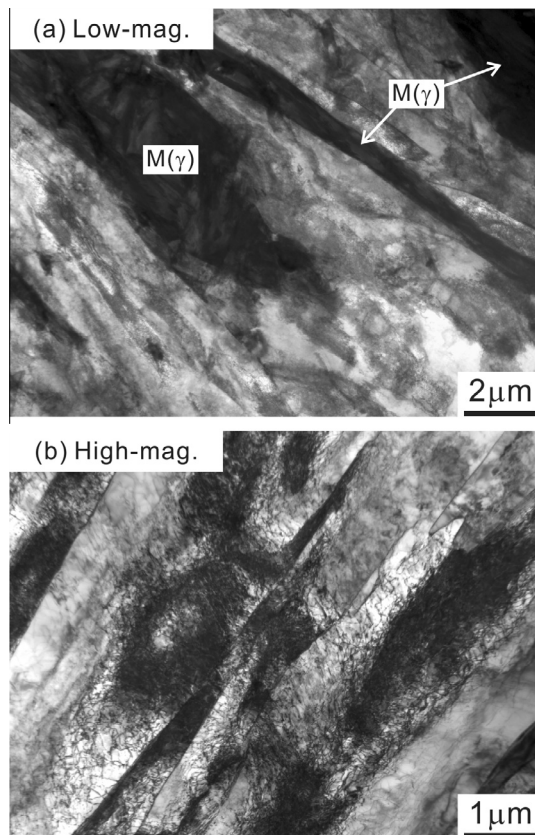

Fig. 6. Dark field TEM images of the samples isothermally transformed at 690 °C for different holding periods: (a) 300 s, (b) 3 h and (c) 48 h. The images were taken under a diffraction condition of $g^* = 200_{VC}$.
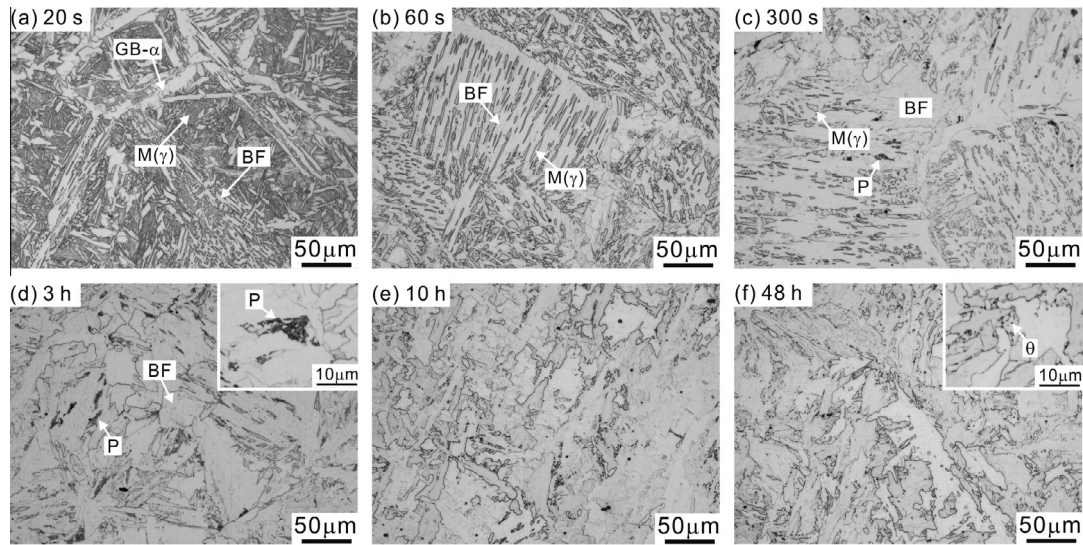
Fig. 7. Optical microstructures of the samples isothermally transformed at 600°C for different holding periods: (a) 20 s, (b) 60 s, (c) 300 s, (d) 3 h, (e) 10 h and (f) 48 h.

Fig. 8. Bright field TEM image of the sample isothermally transformed at 600 °C for 300 s. (a) Low-magnification image, showing a mixture of bainite and martensite. (b) High-magnification image, showing a lath-shaped bainitic ferrite structure with a high density of dislocations.

Fig. 10. The small asterisk indicates that the sample is partially transformed, i.e. containing some amount of martensite. The hardness of the as-quenched sample was determined to be 370 HV, in good agreement with the

hardness of martensite containing 0.1 mass% C [25]. In the case of transformation at 690 °C, 300 s holding led to completion of ferrite transformation (see Fig. 2c). The hardness of this sample is determined to be 280 HV. After the holding for 300 s, the hardness of the samples gradually decreases with increasing the holding period. This result suggests that most of the supersaturated carbon and vanadium atoms in austenite phases have been precipitated as VC particles during interphase precipitation. In other words, the precipitation behavior after the interphase precipitation is already in the over-aged stage. On the other hand, in the case of bainite transformation at 600°C, the hardness shows almost constant until the holding for 30 min (1.8 ks), but it starts to increase with the holding period from 1 h (3.6 ks) to 10 h (36 s), followed by a slight decrease in the holding for 24 h (86.4 ks) and 48 h (172.8 ks). This observation is in good agreement with the precipitation behavior shown in Fig. 9. Namely, the increase in hardness is due to the precipitation of VC particles, so-called secondary hardening. On the other hand, the slight decrease in the hardness by long-time holding suggests that precipitation behavior is in the over-aging stage. The almost constant hardness observed in the early stage until the 30 min holding could be the simultaneous effect of the decrease in strength by the decrease in the volume fraction of martensite and the increase in strength by VC precipitation in bainite.

3.3.2. Stress–strain behavior

Uniaxial tensile tests at room temperature were carried out to understand the effect of nano-sized alloy carbides on strength and ductility of the samples. Fig. 11a and b shows representative nominal stress–strain curves for samples transformed at 690 °C and 600 °C, respectively, for different holding periods. From these stress–strain curves, 0.2% proof stress (or yield stress) ($\sigma_{0.2}$), ultimate tensile strength (UTS) (σ_{UTS}), uniform elongation (e_{unifom}) and total elongation (e_{total}) were determined and plotted in Fig. 12.

Stress–strain curves of 690 °C-transformed samples, which have single phase ferrite structures with nano-sized
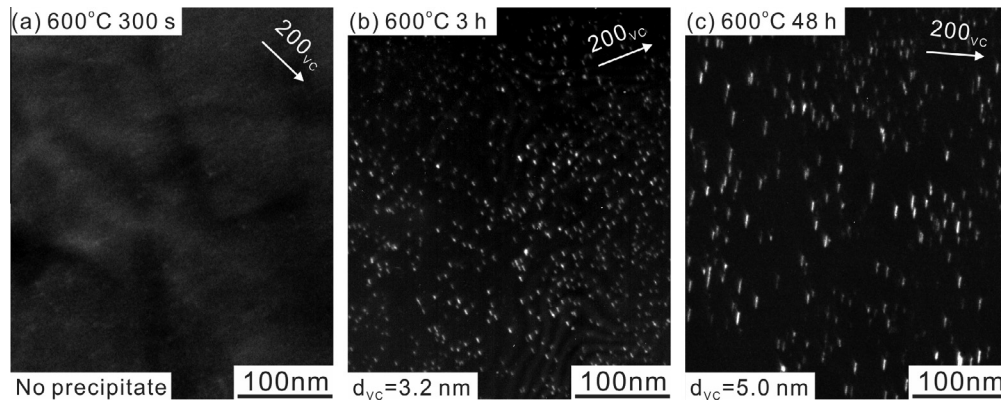
Fig. 9. Dark field TEM images of the samples isothermally transformed at 600 °C for different holding periods: (a) 300 s, (b) 3 h and (c) 48 h. The images were taken under a diffraction condition of $g^* = 200_{VC}$.

carbides, are shown in Fig. 11a. In the ferrite sample with the VC diameter of 4.5 nm, transformed at 690 °C for 300 s, the yield stress is high (640 MPa), but gradual work hardening takes place after yielding, leading to a UTS of 830 MPa. Both uniform and total elongations are relatively large: uniform elongation of 10% and total elongation of 20%. As the holding period increases, i.e. the carbide size becomes larger, the strength gradually decreases (Fig. 12a), in good agreement with the change in the hardness in Fig. 10. It is interesting to note that both uniform and total elongation do not change so much with respect to the holding period (Fig. 12b). A similar tendency has also been observed in Ti,Mo-added low carbon steels composed of ferrite single phase structures with nano-sized alloy carbides [22]. This indicates that interphase precipitated samples with a smaller VC size show higher strength while keeping sufficient elongation.

A general tendency of stress–strain curves in 600 °C-transformed samples dominated by bainite structures in Fig. 11b is quite similar to that in ferrite single phase samples. In all cases, the yield stress is very high but work hardening is relatively small. However, the change in strength with increasing the holding period is different from the ferrite samples. The yield stress is quite high, even in a sample with no precipitate, definitely due to a high density of dislocations, high-angle boundaries (so-called block boundaries [26]) and low-angle lath boundaries. The strength increases first by 3 h holding and then decreases by 48 h holding

(Fig. .12a), corresponding well with the result of hardness in Fig. 10. The increase in strength should mainly be due to the precipitation of VC particles, and the decrease in the later stage would correspond with the coarsening of VC particles, as was mentioned above. It should be emphasized that the elongation in ferrite and bainite samples is quite large, as high as 10% in uniform elongation and 20% in total elongation, almost identical and constant, independent of transformation temperature as well as holding period.
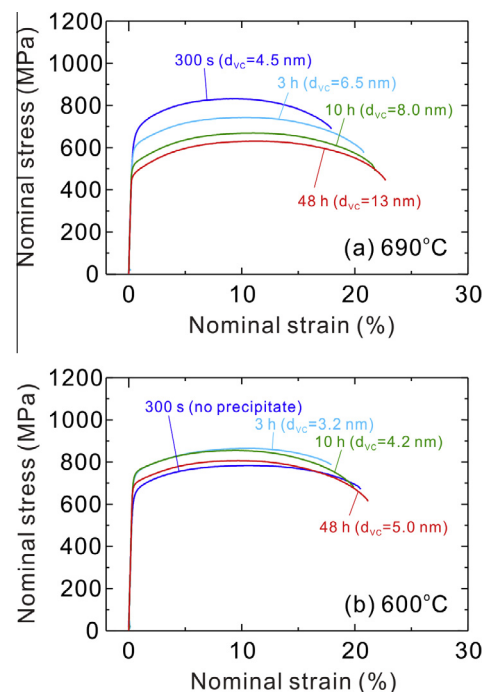
4. Discussion

4.1. Characteristics of stress–strain curves in ferrite and bainite samples with nano-precipitates

The above results demonstrate that both ferrite and bainite samples with nano-precipitates reveal qualitatively
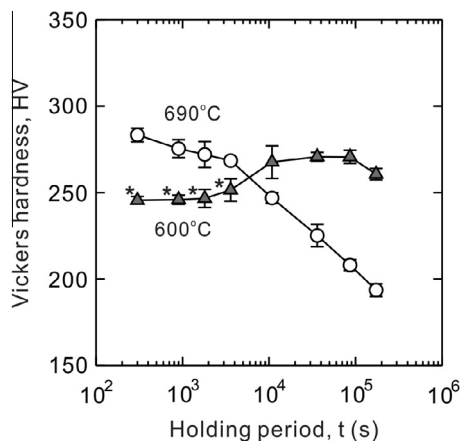
Fig. 10. Vickers hardness of the samples isothermally transformed at 690 °C and 600 °C for different holding periods.

Fig. 11. Nominal stress–strain curves of the samples isothermally transformed at 690 °C and 600 °C for different holding periods. The average diameter of vanadium carbides is indicated in the figure.
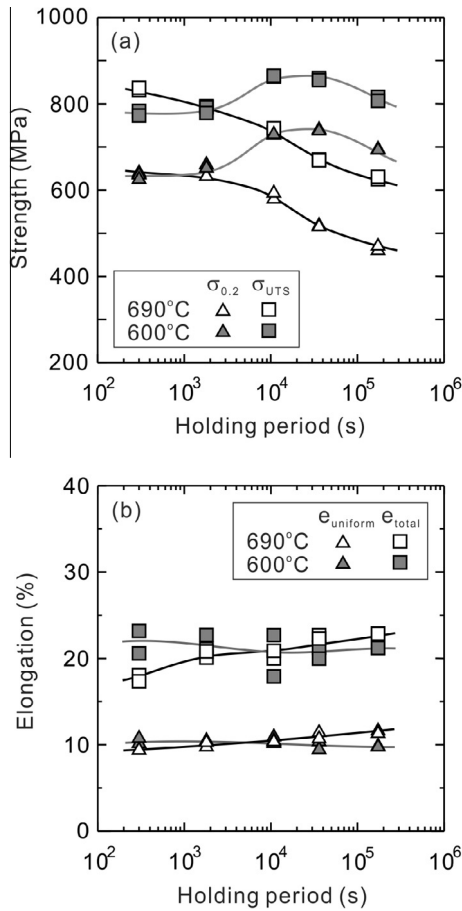
Fig. 12. Strength and ductility of the samples isothermally transformed at 690 °C and 600 °C for different holding periods. 0.2% proof stress ($\sigma_{0.2}$) and UTS (σ_{UTS}) are plotted in (a), and uniform elongation ($e_{uniform}$) and total elongation (e_{total}) are plotted in (b).

similar characteristics in stress–strain curves, i.e. accompanied by high strength, relatively low work hardening and large ductility (Fig. 11). However, the yield stress and UTS varied depending on the matrix structure as well as precipitation structure (Fig. 12). In this section, the effect of matrix structure on the mechanical properties is first discussed, by carefully comparing two selected curves from ferrite and bainite samples with a similar size of VC particles.

Fig. 13 indicates the comparison of stress–strain curves between ferrite and bainite samples with almost identical VC particle diameter. The ferrite curve corresponds to the sample transformed at 690 °C for 300 s, while the bainite curve corresponds to the sample transformed at 600 °C for 10 h. The diameter of VC particles is 4.5 nm in the ferrite sample and 4.2 nm in the bainite sample. It is seen that the yield stress of the bainite sample (~740 MPa) is much higher than that of the ferrite sample (~630 MPa). However, there is no significant difference in the flow stress at a strain of 5% and above. For instance, the UTS in both samples is similar; 830 MPa and 850 MPa in the ferrite and bainite samples, respectively. This result implies that the work hardening after the macroscopic yielding occurs more significantly in the ferrite sample than in the bainite sample, but that the flow stress in the later stage of tensile deformation becomes identical. Another interesting finding is that both uniform and total elongations are almost

identical, independent of the ferrite matrix structure, even independent of the diameter of VC particles (see Fig. 12b).

Such similarities and differences in the stress–strain behavior between ferrite and bainite samples should be due to the precipitation behavior of VC particles in the structures, as has been observed, but other structural factors in the ferrite matrix, such as dislocations and grain boundaries, also have to be taken into account to understand the mechanical behavior. In the following, correlation between microstructures and mechanical properties is discussed in detail, in particular focusing on the effect of nano-sized alloy carbides and ferrite matrix structure on yield stress, work hardening and ductility.

### 4.2. Strengthening mechanisms

The strengthening mechanisms of ferrite and bainite samples with nano-sized carbides are first discussed. To understand the correlation between microstructures and yield stress, the structure-based strength calculation model is used to estimate the theoretical strength. It is assumed here that yield stress ($\sigma_{0.2}$) of the samples can be given by a simple sum of strengthening contribution from individual crystal defects that act as obstacles for dislocation slip in the following equation:

$$\sigma_{0.2} = \sigma_0 + \sigma_{ss} + \sigma_{gb} + \sigma_{dis} + \sigma_{ppt} \ (\text{MPa}) \qquad (3)$$

where σ_0 is friction stress of single crystal pure iron (=53.9 MPa [27]), σ_{ss}, σ_{gb}, σ_{dis} and σ_{ppt} are contributions from solid solution strengthening, grain boundary strengthening, dislocation strengthening and precipitation strengthening, respectively. For both ferrite and bainite samples, fully-transformed samples were only considered for analysis, and a small fraction of pearlite structures is assumed not to affect the strength of materials. To calculate each strengthening contributions, several assumptions are taken into account as described in detail below.

4.2.1. Solid solution strengthening

For ferrite samples, it can be considered that solute carbon atoms in the ferrite matrix are negligibly small, if it is assumed that carbon atoms are almost precipitated as VC particles. In addition, for bainite samples it has been seen in Figs. 10 and 12a that the strength reached the maximum in the holding for 3 h, followed by a slight decrease in 48 h holding. This indicates, as mentioned before, that the precipitation behavior is in the over-aging state, and that solute carbon content in the bainite matrix is also negligible. Therefore, solid solution strengthening σ_{ss} in this
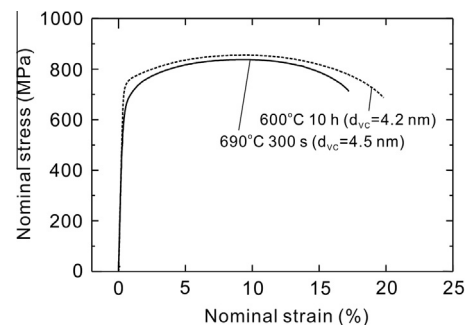
Fig. 13. Comparison of stress–strain curves between ferrite and bainite samples with a similar diameter of VC particles.

calculation can be obtained by considering only the effect of Si and Mn atoms, using a regression equation proposed by Pickering [27]:

$$\sigma_{ss} = 83.2 \times (\text{mass\%Si}) + 32.3 \times (\text{mass\%Mn}) \ (\text{MPa}) \qquad (4)$$

Since the chemical compositions of Si and Mn in the V-added steel are 0.22 mass% and 0.83 mass%, respectively, σ_{ss} is estimated to be 45.1 MPa.

4.2.2. Grain boundary strengthening

Grain boundary strengthening σ_{gb} is calculated from an experimentally-determined Hall–Petch equation for an ultralow carbon interstitial free (IF) steel [22]. Some previous studies [28–30] have reported that even low-angle dislocation boundaries with misorientation angles of 2–5° and above may act as conventional grain boundaries and contribute to strength based on the Hall Petch strengthening. Therefore, in this paper, boundaries with misorientation angles of 2° and above are taken into account as grain boundary strengthening. The grain boundary strengthening is given by

$$\sigma_{gb} = 210 d_{\theta>2°}^{-1/2} \ (\text{MPa}) \qquad (5)$$

where $d_{\theta>2°}$ (μm) is the average spacing of boundaries above 2° determined by the intercept method with random test lines in the EBSD analysis.

4.2.3. Dislocation strengthening

For dislocation strengthening calculation, the Bailey–Hirsch relationship [31] is used:

$$\sigma_{dis} = M\alpha Gb\sqrt{\rho_{total}} \ (\text{MPa}) \qquad (6)$$

where M is the Taylor factor (=2.75 for random textured bcc metals [32]), α is a constant (=0.38 in bcc iron [33]), G is the shear modulus (=81.6 GPa [34]), b is the Burgers vector (=0.248 nm) and ρ_{total} is the total dislocation density. It should also be noted that in bainite samples many lath boundaries with very low misorientation angles are present in the structure, and these lath boundaries are considered to be an array of dislocations. In this calculation, dislocations in the low-angle lath boundaries are assumed to act as dislocation strengthening. The total dislocation density ρ_{total} is equal to the sum of dislocation density between the lath boundaries ρ_0 and in the lath boundaries with misorientation angles below 2° $\rho_{\theta<2°}$. The dislocation strengthening can therefore be expressed as

$$\sigma_{dis} = M\alpha Gb\sqrt{\rho_0 + \rho_{\theta<2°}} \ (\text{MPa}) \qquad (7)$$

The dislocation density between the lath boundaries ρ_0 was determined by TEM observations. The following equation [28] was used to determine the dislocation density in the lath boundaries $\rho_{\theta<2°}$:

$$\rho_{\theta<2°} = \frac{1.5 S_{v,\theta<2°} \theta_{ave,\theta<2°}}{b} \ (\text{m}^{-2}) \qquad (8)$$

where $S_{v,\theta<2°}$ and $\theta_{ave,\theta<2°}$ are the surface area and the average misorientation angle of low-angle boundaries below 2°, respectively. In this calculation, boundaries with misorientation angles below 2° are assumed to be lath boundaries, so that $S_{v,\theta<2°}$ can be given by:

$$S_{v,\theta<2°} = (1 - f_{\theta>2°}) S_{v,total} \ (\text{m}^{-1}) \qquad (9)$$

where $S_{v,total}$ is the surface area of all boundaries, and $f_{\theta>2}^°$ is the fraction of boundaries above 2°. Note that $S_{v,total}$

is equal to $2/d_{all}$, and $f_{\theta>2°}$ can be assumed to be $d_{all}/d_{\theta>2°}$, where d_{all} is the average spacing of all boundaries determined by the TEM images, and $d_{\theta>2°}$ is the average spacing of boundaries above 2° determined by the EBSD measurement. Eq. (9) can therefore be expressed by:

$$S_{v,\theta<2°} = \frac{2}{d_{all}} \left(1 - \frac{d_{all}}{d_{\theta>2°}}\right) \ (\text{m}^{-1}) \qquad (10)$$

Substituting Eq. (10) into Eq. (8), the dislocation density in the lath boundaries is given by:

$$\rho_{\theta<2°} = \frac{3}{bd_{all}} \left(1 - \frac{d_{all}}{d_{\theta>2°}}\right) \cdot \theta_{ave,\theta<2°} \ (\text{m}^{-2}) \qquad (11)$$

Finally, the dislocation strengthening can be obtained by:

$$\sigma_{dis} = M\alpha Gb\sqrt{\rho_0 + \frac{3}{bd_{all}} \left(1 - \frac{d_{all}}{d_{\theta>2°}}\right) \cdot \theta_{ave,\theta<2°}} \ (\text{MPa}) \qquad (12)$$

In this study, the average misorientation angle of boundaries below 2° $\theta_{ave,\theta<2°}$ has not experimentally been measured but is assumed to be 1° for calculation.

4.2.4. Precipitation strengthening

The Orowan mechanism or the Ashby–Orowan mechanism has often been used to explain the precipitation strengthening by hard particles. Precipitation strengthening by the Orowan and the Ashby–Orowan mechanisms are given by Eq. (13) [35,36] and Eq. (14) [37,38], respectively:

$$\sigma_{ppt,Orowan} = \frac{0.8 MGb}{L_{VC}} \ (\text{MPa}) \qquad (13)$$

$$\sigma_{ppt,Ashby-Orowan} = \frac{0.8 MGb}{2\pi\sqrt{1 - vL_{VC}}} \ln\left(\frac{x}{2b}\right) \ (\text{MPa}) \qquad (14)$$

where v is the Poisson's ratio (=0.293 in bcc iron [34]), L_{VC} is the average inter-particle spacing and x is the average particle diameter on the slip planes. The conventional Orowan precipitation strengthening in Eq. (13) has been derived assuming that line energy of dislocation per length is approximated as $Gb^2/2$, while the Ashby–Orowan precipitation strengthening in Eq. (14) has been derived considering more precise line energies of bowed-out edge or screw dislocations around the particle. L_{VC} and x are given by the following equations, assuming that particles are randomly distributed in the matrix [39]:

$$L_{VC} = \sqrt{\frac{2}{3}} \left(\sqrt{\frac{\pi}{f}} - 2\right) \cdot r_{VC} \ (\text{m}) \qquad (15)$$

$$x = 2\sqrt{\frac{2}{3}} \cdot r_{VC} \ (\text{m}) \qquad (16)$$

where r_{VC} (=$d_{VC}/2$) is the average radius and f is the volume fraction of VC particles. For the calculation, the average radius of VC particles determined by the TEM images in Fig. 6 was used, and the volume fraction of VC particles was obtained from the calculation in the Thermo-Calc software, where the equilibrium volume fraction was determined to be 0.47% in the V-added steel. One may argue that sheet spacing of interphase precipitation could strongly affect the precipitation strengthening. This would be true if the inter-particle spacing of nano-precipitates on the precipitation sheets were much smaller than the

sheet spacing. However, in the present case, for the ferrite sample with the average VC diameter of 4.5 nm, the inter-particle spacing of VC particles on a precipitation sheet is estimated to be 22 nm, comparable to the sheet spacing (20–30 nm, see Fig. 3). As the diameter of VC particles becomes larger, the inter-particle spacing of VC particles on the sheets becomes much larger. Therefore, random distribution of VC particles should be a reasonable assumption in the present analysis and discussion.

It should be noted from previous research [21,22,38] that the conventional Orowan mechanism in Eq. (13) overestimates the precipitation strengthening from nano-sized particles while the Ashby–Orowan mechanism in Eq. (14) can reasonably explain the strengthening at least in the average particle diameter range of 3–20 nm. Therefore, for nano-sized VC particles in the present study the Ashby–Orowan mechanism is assumed to operate dominantly for both ferrite and bainite structures.

Using the above proposed equations, strengthening contributions are calculated based on the structural parameters quantified by microstructural observations and analysis. The obtained structural parameters are listed in Table 1. Assuming that Eq. (3) is valid, theoretical yield stress $\sigma_{0.2,cal}$ is calculated and compared with the experimentally-obtained yield stress $\sigma_{0.2,exp}$ in Fig. 14. Each strengthening contribution is listed in Table 2. It is seen in the ferrite samples that the calculated yield stress shows a relatively good agreement with the experiments (Fig. 14a), corresponding well with the previous works [21,22,38].

On the other hand, the calculated yield stress for the bainite samples is much higher than the experiment (Fig. 14b). In particular, strengthening contributions from dislocations and precipitates seem to be over-estimated significantly. It should be noted here that the bainite samples have a high density of both dislocations and nano-sized vanadium carbides. The total dislocation density in the bainite samples has been determined to be $1.5–1.8 \times 10^{14}$ m^{-2}, corresponding to an average dislocation spacing of ~70–80 nm if the average spacing is assumed equal to $\rho_{dis}^{-1/2}$ (see Table 1). On the other hand, the average inter-particle spacing of vanadium carbides is ~30–50 nm in these samples (see Table 1). Therefore, both dislocations and nano-sized carbides are narrowly distributed each other. The overestimation in strength calculation for bainite samples indicates that strengthening contributions from dislocations and

precipitates cannot simply be additive in such a situation where the spacing of dislocations and precipitates is very small. In that case, an alternative equation has been proposed to calculate the strength [40,41], i.e. by the square root of the sum of squares of strengthening contributions from dislocations and precipitates:

$$\sigma_{dis+ppt} = \sqrt{\sigma_{dis}^2 + \sigma_{ppt}^2} \text{ (MPa)} \tag{17}$$

This equation has been derived by taking account of the effective spacing of dislocations and precipitates, both of which act as short-range obstacles against moving dislocations. The total strength can therefore be obtained as

$$\sigma_{0.2} = \sigma_0 + \sigma_{ss} + \sigma_{gb} + \sqrt{\sigma_{dis}^2 + \sigma_{ppt}^2} \text{ (MPa)} \tag{18}$$

The calculated strength using Eq. (18) is shown in Table 2 and Fig. 15b, where very good agreement has been obtained between the experiments and calculation for the bainite steels. The calculation by Eq. (18) has also been applied for the ferrite samples in Fig. 15a. In the ferrite samples, the calculated strength by Eq. (18) is also in good agreement with the experiments, as for the calculation by Eq. (3).

The above analysis can lead to the following conclusions. Precipitation strengthening from nano-sized alloy carbides is explained by the Ashby–Orowan mechanism, at least in the average particle diameter of 3 nm and larger, in both ferrite and bainite samples. To understand the experimentally-measured yield stress, solid solution strengthening and grain boundary strengthening can simply be additive, but contributions from dislocations and precipitates have to be averaged by the square root of the sum of squares of two contributions, no matter whether the ferrite matrices are polygonal ferrites with few dislocations or lath-shaped bainitic ferrites with a high density of dislocations. The reason why calculated strength from both Eqs. (3) and (18) shows a relatively good agreement with the experiments in the ferrite samples would be the fact that strengthening contribution from precipitates is quite large compared with that from dislocations. This is mathematically reasonable, since $\sqrt{\sigma_{dis}^2 + \sigma_{ppt}^2}$ becomes closer to $\sigma_{dis} + \sigma_{ppt}$ when σ_{ppt} is much larger than σ_{dis}. If you consider the physical meaning of how both dislocations and precipitates affect dislocation movement, it should be more reasonable to use Eq. (18) for estimating the strength of samples, instead of using Eq. (3).

Table 1. Structural parameters of the samples transformed at 690 °C or 600 °C for different holding periods.

Sample	$d_{\theta>2deg}$ μm	d_{all} μm	ρ_0 m^{-2}	$\rho_{\theta<2deg}$ m^{-2}	ρ_{total} m^{-2}	L_{dis} nm	d_{VC} nm	L_{VC} nm
Transformed at 690 °C (Ferrite)								
300 s	29	–	2.7×10^{13}	–	2.7×10^{13}	190	4.5	44
3 h	29*	–	8.0×10^{13}	–	8.0×10^{13}	110	6.5	63
10 h	29*	–	5.6×10^{13}	–	5.6×10^{13}	130	8.0	78
48 h	29	–	5.3×10^{13}	–	5.3×10^{13}	140	13	130
Transformed at 600 °C (Bainite)								
3 h	5	2.9	1.5×10^{14}	3.1×10^{13}	1.8×10^{14}	74	3.2	32
10 h	5*	2.8	1.6×10^{14}	3.2×10^{13}	1.9×10^{14}	72	4.2	41
48 h	5*	2.9	1.2×10^{14}	3.0×10^{13}	1.5×10^{14}	81	5.0	53

* The EBSD measurements have not yet been carried out for the samples with the asterisk, and therefore the average spacing of boundaries with misorientation angle above 2° were not experimentally obtained. In this calculation, the average spacing $d_{\theta>2deg}$ of 29 μm and 5 μm are used for the ferrite and bainite samples, respectively, assuming that no significant boundary migration took place during long-time holding.
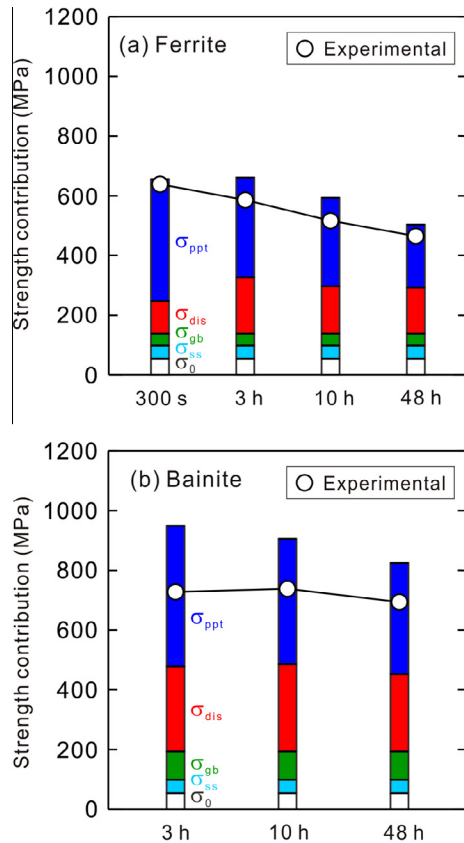
Fig. 14. Comparison between the calculated and experimentally-obtained yield stress. Contributions from solid solution strengthening, grain boundary strengthening, dislocation strengthening and precipitation strengthening were calculated using Eqs. (4), (5), (12) and (14), and it is assumed that each contribution can simply be additive based on Eq. (3).

4.3. Effect of nano-precipitates and ferrite matrix structure on tensile ductility

As was demonstrated in Figs. 11 and 12, both ferrite and bainite samples showed quite similar behavior in elongation. Namely, the uniform and total elongation is approximately 10% and 20%, respectively, independent of the ferrite matrix structure as well as VC particle size. It is somewhat surprising since the ferrite matrix in the initial state is significantly different between the ferrite and bainite samples: the ferrite samples are composed of coarse equiaxed ferrite grains with few interior dislocations, while the bainite samples are composed of narrowly spaced bainitic lathes with a high density

of dislocations. In this section, work hardening behavior of ferrite and bainite samples with nano-precipitates are discussed and correlated with ductility of the samples.

4.3.1. Work hardening rate

To understand the ductility of the samples, work hardening rates are compared in Fig. 16 for almost fully transformed samples with nano-precipitates. For the ferrite samples (Fig. 16a), the work hardening rate in the early stage of deformation is larger as the carbide size is smaller. However, in the later stage of deformation, there is no big difference in the work hardening rate regardless of the VC size. It is seen that for all three curves, work hardening rate starts to decrease gradually at a true strain of ∼0.02, and the onset of plastic instability is retarded, leading to a relatively large uniform elongation (∼10%, see Fig. 12b). For the bainite samples (Fig. 16b), no significant difference can be observed between those three samples, which is probably due to the fact that there is no big difference in microstructural features, i.e. bainite block size, lath size, dislocation density and VC particle size, between these samples (see Table 2). As for the ferrite samples, the decrease in work hardening rate seems to be retarded in the later stage of tensile deformation also in the bainite samples. In order to directly see the difference in work hardening between ferrite and bainite samples, two selected samples of work hardening rate are compared in Fig. 16c, where two curves are from the same samples shown in Fig. 13, i.e. both samples have an identical diameter of VC particles of 4–5 nm. It is seen that the work hardening rate in the ferrite sample is higher than in the bainite sample in the early stage of tensile strain, but the onset of plastic instability occurred at a similar strain. It should also be noted that the flow stress at the onset of plastic instability is almost the same. Such tendencies are in good agreement with the observations in the stress–strain curves in Fig. 13.
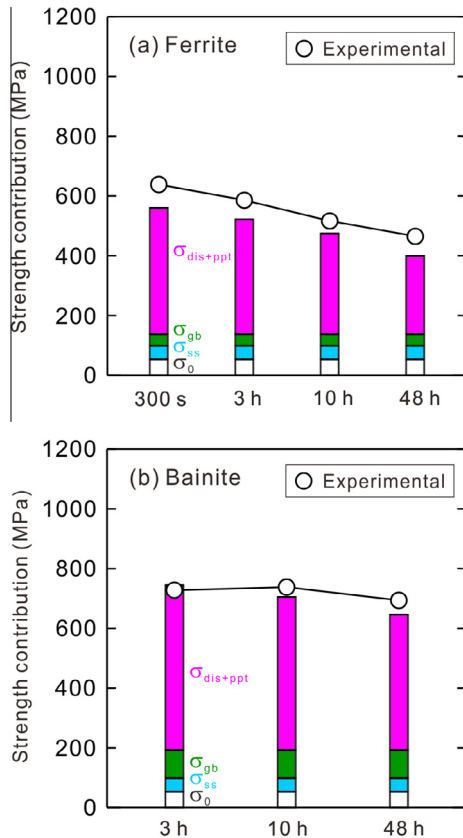
4.3.2. Dislocation structures

To further understand the observed work hardening behavior of the samples, dislocation structures developed during tensile tests were observed by TEM for some selected samples. The samples were deformed in tension, interrupted at different plastic strains, unloaded and subjected for the TEM observations. For the ferrite samples, the samples transformed at 690 °C for 300 s and for 48 h were chosen, where the average diameter of VC particles of these samples is 4.5 nm and 13 nm, respectively. For the bainite sample, the sample transformed at 600 °C for 10 h, with an average VC diameter of 4.2 nm, was chosen to be observed. For comparison, results from an ultralow carbon IF steel with an average ferrite grain size of 54 μm

Table 2. Experimentally-obtained and calculated strength of the samples transformed at 690 °C or 600 °C for different holding periods.

| Sample	s_{exp} MPa	σ_0 MPa	σ_{ss} MPa	σ_{gb} MPa	σ_{dis} MPa	σ_{ppt} MPa	$\sigma_{0.2,cal}$ (Eq. 3) MPa	$\sigma_{0.2,cal}$ (Eq. 18) MPa
Transformed at 690 °C (Ferrite)								
300 s	634	53.9	45.1	39	110	385	632	538
3 h	586	53.9	45.1	39	189	315	642	506
10 h	517	53.9	45.1	39	159	280	577	460
48 h	465	53.9	45.1	39	154	200	492	390
Transformed at 600 °C (Bainite)								
3 h	728	53.9	45.1	94	285	445	923	722
10 h	739	53.9	45.1	94	293	397	882	686
48 h	694	53.9	45.1	94	260	350	803	629

Fig. 15. Comparison between the calculated and experimentally-obtained yield stress. In this calculation, dislocation strengthening and precipitation strengthening were first calculated using Eqs. (12) and (14), and these two contributions were averaged using Eq. (17).

[22] are also demonstrated to emphasize the effect of nano-sized carbides. Fig. 17a and b shows TEM images of the ferrite sample with the carbide diameter of 4.5 nm and the bainite sample with the carbide diameter of 4.2 nm after 1% tensile plastic strain, as examples. The dislocation structure after 1% tensile strain for the IF steel sample is also indicated in Fig. 17c. For both ferrite and bainite samples in Fig. 17a and b, dislocations are uniformly distributed in the observed areas, although the IF steel sample shows a quite inhomogeneous distribution of dislocations. Dislocation density has been determined to be 1.9×10^{14} m^{-2} in the ferrite sample and 2.7×10^{14} m^{-2} in the bainite samples, respectively, i.e. the bainite sample has a higher dislocation density than the ferrite sample after 1% strain. Compared with these two samples, the dislocation density in the IF steel sample (5.8×10^{13} m^{-2}) is much lower.

The change in dislocation density is summarized as a function of tensile strain in Fig. 18. The dislocation density gradually increases with increasing the strain in the IF steel sample. However, in the ferrite samples with nano-sized carbides the density increases more rapidly than in the IF steel. There is a tendency that the sample with a finer particle size leads to a more rapid increase in dislocation density during tensile test. These observations suggest that nano-sized VC particles act as sites for dislocation multiplications, and finer particles are more effective to multiply dislocations. On the other hand, the bainite sample has a higher dislocation density in the initial state, but an increase in the dislocation density with applied strain
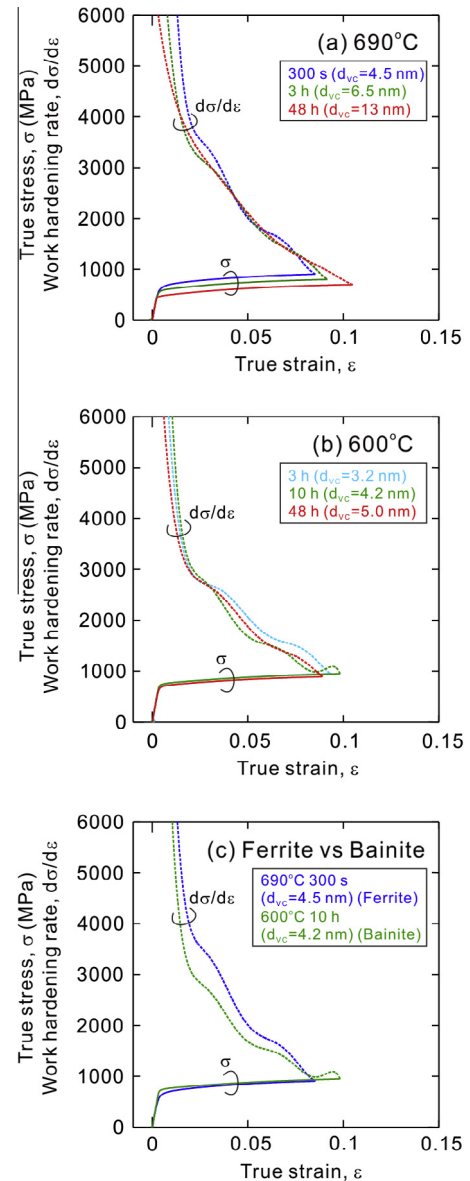

Fig. 16. True stress–strain curve and work hardening rate for the ferrite and bainite samples. The holding period and average diameter of vanadium carbides are also indicated in the figure.

occurs very fast as well. It is interesting that the dislocation density after 5% or ∼10% strain is identical between the ferrite (690 °C, 300 s) and bainite sample (600 °C, 10 h). However, it is also demonstrated that in these two samples an increase in the dislocation density becomes slow in the later stage of deformation, indicating that dynamic recovery occurs significantly [22]. Similar tendency in dislocation structure development has been observed in low carbon steels with nano-sized (Ti,Mo)C particles [22,42].

4.3.3. Possible mechanisms of work hardening

From the above observations, the work hardening and ductility of the samples are discussed in the following. If tensile stress is applied to ferrite samples with nano-precipitates, the nano-precipitates act as strong obstacles for dislocation glide, leading to a very high yield stress, predominantly due to large precipitation strengthening by the Ashby–Orowan mechanism, as discussed in Section 4.1.
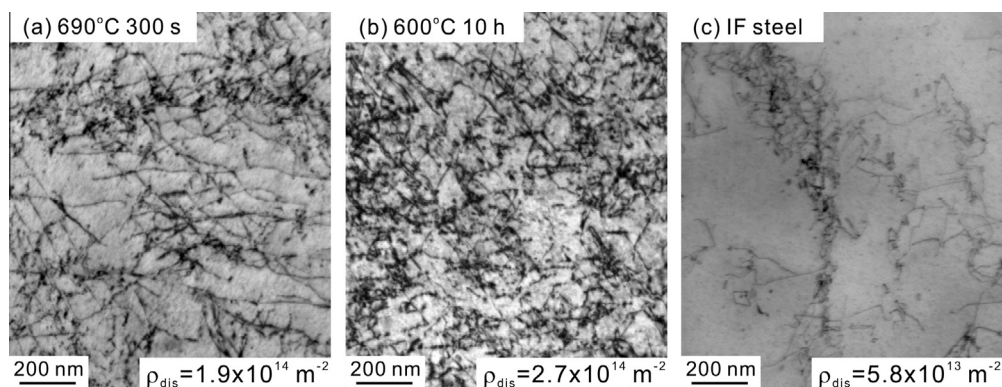
Fig. 17. Dislocation structures after tensile strain of 1% for the ferrite and bainite samples with nano-sized carbides: (a) 690 °C 300 s (d_{VC} = 4.5 nm) and (b) 600 °C 10 h (d_{VC} = 4.2 nm). The result of an IF steel with no VC particles is also indicated for comparison in (c).

When dislocations pass through the nano-sized carbides, moving dislocations may leave dislocation loops, so-called Orowan loops, around the particles, as observed in the Ti,Mo-added low carbon steels with nano-sized carbides [22]. These dislocation loops would reduce an effective inter-particle spacing or produce a large internal stress, both of which may act as further strong obstacles for trailing moving dislocations. In such a situation, dislocations with secondary slip systems may easily be activated, or cross slips of primary dislocations may also occur in further plastic deformation. Interaction of such dislocations may cause an enhanced dislocation multiplication in the beginning of tensile deformation, as observed in Fig. 17. This should be the reason why a larger work hardening rate is observed when the diameter of VC particles is smaller in the early stage of deformation (see Fig. 16a). These results clearly suggest that nano-precipitates finely and uniformly distributed in the ferrite matrix act as sources for dislocation multiplication. On the other hand, since the density of nano-sized carbides are very high, multiplied dislocations in the vicinity of particles may easily interact and annihilate each other. Therefore, dynamic recovery could be enhanced in the later stage of deformation, in good agreement with the fact that an increase in dislocation density becomes slower in the later stage of tensile test in the 690 °C–300 s sample (Fig. 18). Such enhanced dynamic

recovery would suppress a rapid increase in the strength, leading to a mild work hardening, and retard the onset of plastic instability. This could be the reason why a relatively large uniform elongation was obtained in the ferrite samples with nano-precipitates (Fig 11a).

In bainite steels, on the other hand, a high density of dislocations, in addition to nano-sized precipitates, should have a significant contribution to an increase in yield stress (see Table 1). When compared with the ferrite sample with a similar diameter of VC particles (Fig. 13), the yield stress is much larger than the ferrite sample, which can be explained mainly by the difference in precipitation and dislocation strengthening (Fig. 15). However, the work hardening rate is lower in the bainite sample than in the ferrite sample just after the yielding (Fig. 16c). This can be understood as follows. Nano-precipitates in the bainite samples may also act as a site for dislocation multiplication, as for the ferrite samples. However, in addition, the bainite sample already has a much higher dislocation density than the ferrite sample in the initial state. Therefore, dislocation annihilation may start to occur in the very early stage of deformation in the bainite sample, while the ferrite sample still has enough room for dislocations to multiply, leading to a larger work hardening in the ferrite sample than in the bainite sample. However, it is interesting to note that the flow curves of these samples become almost identical at ~5% strain and above (Fig. 13). This result corresponds well with the observation in Fig. 18 that dislocation density in the ferrite and bainite samples with the average VC diameter of ~5 nm is quite similar. In other words, the flow stress of these samples can basically be explained by the work hardening by dislocation multiplication during tensile testing.

Another interesting observation is that post-uniform elongation is also relatively large; ~10%, independent of ferrite matrix structure as well as diameter of VC particles (Figs. 11 and 12). This phenomenon could also be understood in terms of enhanced dynamic recovery. If it is assumed that enhanced dynamic recovery continues to occur even after necking, dislocation accumulation and stress concentration may be retarded, and therefore void or crack formation would be suppressed. This can be one of the explanations why the ferrite samples with nano-sized carbides as well as the bainite samples show a quite large post-uniform elongation. To verify the above hypothesis, the formation and propagation of voids or cracks have to be investigated in detail for nano-precipitated steels, which will be our future work.
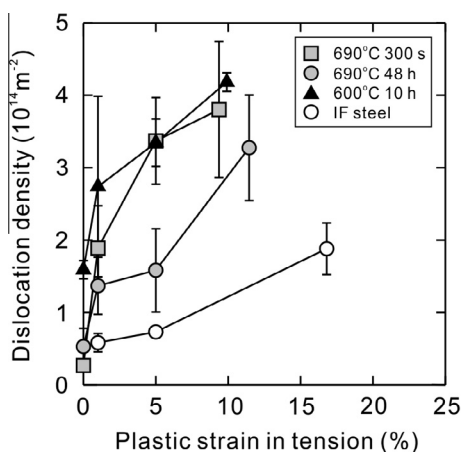
Fig. 18. Dislocation density during tensile test in the ferrite and bainite samples with nano-sized vanadium carbides. The result for an IF steel is also indicated for comparison.

5. Conclusions

In this work, stress–strain behavior of ferrite and bainite samples with nano-precipitates was systematically investigated using a V-added low carbon steel, and the effect of nano-precipitation on yield stress, work hardening behavior and ductility of the samples was discussed in detail. The obtained results are summarized as follows.

(1) Ferrite samples with nano-sized vanadium carbides were produced by interphase precipitation, while bainite samples with vanadium carbide particles were obtained by bainite transformation followed by aging. The stress–strain behaviors were characterized by high yield stress, relatively low work hardening and large elongation, in both ferrite and bainite samples regardless of the ferrite matrices. In samples with an identical diameter of VC particles, the yield stress of the ferrite sample is lower than that of the bainite sample, but the work hardening is larger in the ferrite sample than in the bainite sample in the beginning of tensile deformation, leading to a similar flow curve in the later stage of deformation.

(2) Good agreement was obtained between the experimentally-obtained yield stress and calculation in both ferrite and bainite samples, where strengthening contributions from solute atoms and grain boundaries are simply additive, while dislocation strengthening and precipitation strengthening are averaged by the square root of the sum of squares of these two contributions.

(3) Nano-precipitates may act as sites for dislocation multiplication and may enhance work hardening in the early stage of tensile deformation. On the other hand, dynamic recovery may be accelerated in the later stage, due to the interaction of multiplied dislocations. Such enhanced dynamic recovery could be responsible for a relatively large ductility in both ferrite and bainite samples.

Acknowledgements

References

[1] Orowan E. Symp, Internal Stresses in Metals and Alloys, Institute of Metals, London, 1948, p. 451.
[2] M.F. Ashby, Z Metallkunde 55 (1964) 5.
[3] T. Epicier, Adv. Eng. Mater. 8 (2006) 1197.
[4] A.T.W. Barrow, P.E.J. Rivera-Díaz-del-Castillo, Acta Mater. 59 (2011) 7155.
[5] A.T. Davenport, F.G. Berry, R.W.K. Honeycombe, Metal. Sci. J. 2 (1968) 104.
[6] S. Freeman, R.K.W. Honeycombe, Metal. Sci. 11 (1977) 59.
[7] R.A. Ricks, P.R. Howell, Acta Metall. 31 (1983) 853.
[8] I.B. Timokhina, P.D. Hodgson, S.P. Ringer, R.K. Zheng, E.V. Pereloma, Scr. Mater. 56 (2007) 601.
[9] H.W. Yen, P.Y. Chen, C.Y. Huang, J.R. Yang, Acta Mater. 59 (2011) 6264.
[10] K. Tomita, Y. Funakawa, T. Shiozaki, E. Maeda, T. Yamamoto, Materia. Jpn. 42 (2003) 70.
[11] T. Shimizu, Y. Funakawa, S. Kaneko, JFE Giho 4 (2004) 22.
[12] N. Iwama, I. Nomura, M. Mori, M. Yano, T. Manabe, Materia. Jpn. 36 (1997) 622.
[13] S. Niwa, I. Machida, T. Katoh, N. Uehara, Y. Tanaka, Denki Seiko 53 (1982) 26.
[14] A.K. Seal, R.W.K. Honeycombe, J. Iron Steel Inst. 188 (1958) 9.
[15] E. Tekin, P.M. Kelly, J. Iron Steel Inst. 203 (1965) 715.
[16] D. Raynor, J.A. Whiteman, R.W.K. Honeycombe, J. Iron Steel Inst. 204 (1966) 349.
[17] R.G. Baker, J. Nutting, J. Iron Steel Inst. 192 (1959) 257.
[18] K.J. Irvine, F.B. Pickering, J. Iron Steel Inst. 187 (1957) 292.
[19] K.J. Irvine, F.B. Pickering, J. Iron Steel Inst. 201 (1963) 54.
[20] R.G. Baker, Nutting J. ISI Special Report 1959; 64: 1.
[21] G. Miyamoto, R. Hori, B. Poorganji, T. Furuhara, ISIJ Int. 51 (2011) 1733.
[22] N. Kamikawa, Y. Abe, G. Miyamoto, Y. Funakawa, T. Furuhara, ISIJ Int. 54 (2014) 212.
[23] T. Hara, K. Tsuchiya, K. Tsuzaki, X. Man, T. Asahata, A. Uemoto, J. Alloys Compd. 577 (2013) S717.
[24] Y.J. Zhang, G. Miyamoto, K. Shinbo, T. Furuhara, Scr. Mater. 69 (2013) 17.
[25] G. Krauss, Mater. Sci. Eng. A 273–275 (1999) 40.
[26] T. Furuhara, H. Kawata, S. Morito, G. Miyamoto, T. Maki, Metall. Mater. Trans. A 39A (2008) 1003.
[27] F.B. Pickering, Physical Metallurgy and the Design of Steels, Applied Science Publishers, London, 1978, p. 63.
[28] D.A. Hughes, N. Hansen, Acta Mater. 48 (2000) 2985.
[29] Q. Liu, X. Huang, D.J. Lloyd, N. Hansen, Acta Mater. 50 (2002) 3789.
[30] N. Kamikawa, X. Huang, N. Tsuji, N. Hansen, Acta Mater. 57 (2009) 4198.
[31] J.E. Bailey, P.B. Hirsch, Phil. Mag. 5 (1960) 485.
[32] G.Y. Chin, W.L. Mammel, Trans. Metall. Soc. AIME 239 (1967) 1400.
[33] A.S. Keh, Phil. Mag. 12 (1965) 9.
[34] G.W.C. Kaye, T.H. Laby, Tables of Physical and Chemical Constants, 14th edn., Longman, London, 1973, p. 31.
[35] E. Orowan, in: M. Cohen (Ed.), Dislocations in Metals, AIME, New York, 1954, p. 69.
[36] A.J.E. Foreman, M.J. Makin, Phil. Mag. 14 (1966) 911.
[37] M.F. Ashby, in: A.S. Argon (Ed.), Physics of Strength and Plasticity, MIT Press, Reading, MA, 1969, p. 113.
[38] T. Gradman, The Physical Metallurgy of Microalloyed Steels, Maney Publishing, London, 2002, p. 47.
[39] A. Kelly, R.B. Nicholson, Prog. Mater. Sci. 10 (1963) 151.
[40] A.J.E. Foreman, M.J. Makin, Canadian J. Phys. 45 (1967) 511.
[41] E. Hornbogen, E.A. Starke Jr, Acta Metall. Mater. 41 (1993) 1.
[42] K. Yamada, H. Nakamichi, K. Sato, K. Yasunaga, T. Daio, S. Matsumura, Tetsu-to-Hagané 98 (2012) 469.